



HAL
open science

Image enhancement with PDEs and nonconservative advection flow fields

Vincent Jaouen, Julien Bert, Nicolas Boussion, Hadi Fayad, Mathieu Hatt,
Dimitris Visvikis

► **To cite this version:**

Vincent Jaouen, Julien Bert, Nicolas Boussion, Hadi Fayad, Mathieu Hatt, et al.. Image enhancement with PDEs and nonconservative advection flow fields. *IEEE Transactions on Image Processing*, 2018, 28 (6), pp.1-1. 10.1109/TIP.2018.2881838 . hal-01941451

HAL Id: hal-01941451

<https://hal.science/hal-01941451v1>

Submitted on 1 Dec 2018

HAL is a multi-disciplinary open access archive for the deposit and dissemination of scientific research documents, whether they are published or not. The documents may come from teaching and research institutions in France or abroad, or from public or private research centers.

L'archive ouverte pluridisciplinaire **HAL**, est destinée au dépôt et à la diffusion de documents scientifiques de niveau recherche, publiés ou non, émanant des établissements d'enseignement et de recherche français ou étrangers, des laboratoires publics ou privés.

Image enhancement with PDEs and nonconservative advection flow fields

Vincent Jaouen*, Julien Bert, Nicolas Boussion, Hadi Fayad, Mathieu Hatt and Dimitris Visvikis, *Senior Member, IEEE*

Abstract—We propose a new method for the progressive enhancement of images degraded by noise and blur using shock filters. The originality of our approach lies in the iterative exploitation of nonconservative edge based force fields normally designed for segmentation to determine both locations and amplitudes of the sharpening action. The proposed Nonconservative Shock Filter (NCSF) produces images with strong discontinuities that can be used as an additional pre-processing step to facilitate higher level tasks such as edge detection or segmentation. NCSF is especially useful when coupled with an anisotropic diffusion equation in noisy configurations. Using the proposed method, edges that are not well defined prior to filtering can be iteratively recovered. We show processing results on various types of images, focusing on medical transrectal ultrasound and brain PET imaging.

Index Terms—Image enhancement, Image sharpening, Denoising, Partial differential equations, Shock filter, Anisotropic diffusion.

I. INTRODUCTION

INITIATED by the non-local means algorithm [1], image denoising techniques aiming at solving the known additive white Gaussian noise (AWGN) model have improved considerably over the past decade, mainly thanks to patch-based approaches. State-of-the-art techniques include block matching and 3D filtering (BM3D) and its variants [2], [3], spatially adaptive iterative singular-value thresholding (SAIST) [4], Non-Local Bayes [5], or online dictionary learning using patches [6] or patch groups [7]. It was recently suggested that modern approaches could be close to reaching a theoretical limit in terms of minimization of the mean square error (MSE) [8], [9], to the point that a recent publication claims that “*to a large extent, removal of zero-mean white additive Gaussian noise from an image is a solved problem in image processing*” [10].

This statement however concerns natural photographic images with high levels of details, at which are devoted most efforts in the image processing community. Other types of images such as medical images, which typically present less details and more noise, are likely to have more room for improvement towards these theoretical bounds [9]. Moreover,

*Asterisk indicates corresponding author.

Authors are with LaTIM, UMR 1101, Inserm, Université de Bretagne Occidentale, Brest University Hospital, 22, Av. Camille Desmoulins, 29200 Brest, France.

This paper has supplementary downloadable material available at <http://ieeexplore.ieee.org>, provided by the author. The material includes additional image restoration experiments performed on natural images. Contact vjaouen@gmail.com for further questions about this work.

alongside noise, medical images are often affected by additional distortions. These include blur, insufficient contrast between regions of interest or artifacts that further complicate higher level processing tasks such as edge detection or segmentation. In these cases, noise suppression is not sufficient and application-specific image alteration is needed. One rather use in this context the concept of *image enhancement* [11], which can be considered as an intermediate processing level between denoising (where mild modification of the original image occurs), and segmentation (where image regions are fully abstracted into independent objects). Among various application contexts, image enhancement may be required in medical images where objects of interest (organs, tumors...) are large compared to the field of view and in which smaller details are artificial or irrelevant for the task at hand. For example, appropriate pre-processing techniques that render macroscopic features more visible may be of practical interest for facilitating user guided image analysis tasks and automated segmentation or co-registration between different imaging modalities. The appropriateness of an enhancement method is entirely dependent on the targeted application, and the ultimate judge of the performance of an enhancement technique is often the user [11]. This is in contrast to the restoration of images corrupted by a known degradation model, where methods can be validated using *full-reference* image quality metrics based on distances to clean images, such as signal-to-noise ratio (SNR) or structural similarity [12].

In this paper, we focus on the common requirement of sharpening image edges while smearing out noise and irrelevant details. We propose a new partial differential equation (PDE)-based filtering formulation by coupling a nonlinear diffusion term and a new regularized shock filter term. By exploiting nonconservative edge flow fields normally designed for active contour segmentation, we iteratively estimate the locations of shocks, that can yield improved sharpening effects. Following a recent work [13], we also reformulate the action of shock filtering as an advection process of the image intensities embedded in external vector fields, allowing for fast approximations of the proposed scheme.

Images obtained after processing with the proposed method compare favorably to state of the art approaches according to both subjective evaluation and quantitative evaluation metrics. In the present case, we focus on edge detection, image sharpness, and segmentation accuracy with application to transrectal medical ultrasound (TRUS) images, as well as the improvement of partial volume corrected positron emission tomography (PET) brain images.

The rest of the article is organized as follows. In the next section, we present current PDE-based approaches for image enhancement and their limitations. Section III describes the proposed shock filter based on nonconservative fields. The validation setup used in our experiments is described in section IV. Results are presented in section V. Finally, conclusions are drawn in section VI.

II. BACKGROUND

In this section, we briefly discuss partial differential equations in image processing and describe related PDE-based enhancement approaches using shock filters.

A. Partial differential equations in image processing

Unlike patch-based approaches that rely on self-similarities of local patches across the image domain, pixel-based regularizers such as Tikhonov [14], Mumford-Shah [15] or total variation (TV) regularization methods [16] rely on the hypothesis that images obey to global generic priors, such as piecewise constancy or piecewise linearity. These priors are often expressed under the variational framework, where the solution image corresponds to the minimization of an energy integrated across the image domain [17].

Most developments in image regularization were made during the 1990s using regularizing PDEs, where image evolution towards a solution is understood as an iterative gradient descent scheme for solving the Euler-Lagrange equation associated with the corresponding variational problem [18], [19]. Since the seminal work on anisotropic diffusion [20], PDE schemes have become a field on their own, and many proposed regularizing PDEs do not necessarily derive from a variational formulation. Under the framework of PDEs, various terms can be combined to obtain different and simultaneous desired effects for the targeted application. Due to this modular nature, they can lead to a wide variety of outputs, ranging from low-level denoising to super-resolution or image segmentation, and are well-adapted to image enhancement [21], [22]. Such schemes allow equally for an easy extension to vector-valued images like color or multimodal images [23]–[25]. For these reasons, while PDEs are generally considered less effective than patch-based approaches for natural image denoising due to their general tendency to smear out image details [7], they are still popular for medical imaging applications [26]–[29].

B. Shock filter

A popular edge sharpening scheme using PDEs is the shock filter (SF), a nonlinear hyperbolic operator that restores shock-like patterns (i.e. sharp discontinuities) in blurred signals. Its general PDE formulation is :

$$\mathcal{I}_t = -\mathcal{S}(\mathcal{L}(\mathcal{I})) \|\nabla \mathcal{I}\| \quad \text{s.t.} \quad \mathcal{I}^0 = \mathcal{I}, \quad (1)$$

where subscript \cdot_t denotes partial derivative with respect to Euler time t , $\mathcal{L}(\mathcal{I})$ is a signed edge indicator function and \mathcal{S} is a sign-preserving function of this edge response. In the original formulation of the SF [30], $\mathcal{S}(x) = \text{sign}(x)$ and $\mathcal{L} = \mathcal{I}_{\eta\eta}$, where η is the direction of the image gradient,

so that shocks are recovered around the zero-crossings of the second directional derivative along the gradient direction. This scheme is extremely unstable due to the sensitivity of the second derivative to noise. For this reason, a PDE scheme in which a Gaussian regularized SF term is coupled to mean curvature flow was previously proposed [31] :

$$\mathcal{I}_t = -\mathcal{S}(G_\sigma * \mathcal{I}_{\eta\eta}) \|\nabla \mathcal{I}\| + c\mathcal{I}_{\xi\xi} \quad \text{s.t.} \quad \mathcal{I}^0 = \mathcal{I}, \quad (2)$$

where ξ is the direction perpendicular to the gradient direction η (isophote direction), G_σ is a Gaussian kernel of scale σ and $*$ is the convolution operation. A SF term was incorporated [32] in the complex diffusion framework [33] to regularize the solution without making use of Gaussian convolution and allowing for a progressive increase of the sharpening effect along with diffusion time. The sign preserving function $\mathcal{S}(x) = \text{sign}(x)$ was also replaced by a softer version $\mathcal{S}(x) = 2 \arctan(ax)/\pi$ to favour sharpening near edges in a nonlinear fashion controlled by parameter a . The use of the *tanh* function [34] or fuzzy memberships functions [35] were also proposed in recent papers.

Recently, an unconditionally stable approximation of the SF was proposed [13] following the observation that its action can be rewritten as the advection of the image intensity values along the flow lines of the (irrotational) vector field:

$$\vec{u} = \frac{1}{2} \nabla \|\nabla \mathcal{I}\|^2. \quad (3)$$

In the context of fast processing of surface meshes, this new formulation is used to approximate the shock filter for any Euler time t by back-tracing image values along the flow lines of \vec{u} .

Despite providing improved performance in noisy configurations over the original SF formulation, all of these methods use regularized versions of the image second derivative as the signed edge response. In this context, robustness to noise can only be improved through increased smoothing, e.g. by using larger values of scale σ in eq. (2) or by smoothing the advection field in eq. (3) [13]. Such smoothing can only be performed at the expense of smearing out weak edges in the image, which is not desirable, especially in medical images.

C. Relationship with active-contour external forces

The vector field \vec{u} of eq. (3) is, up to a factor 1/2, the gradient of the scalar edge map $\|\nabla \mathcal{I}\|^2$. This is the classical conservative (i.e. irrotational) edge-based force-field (EBF) used for active contour segmentation [36]. This observation is of interest as it allows for a natural connection between shock filtering and the vast amount of work made on EBF in the active contours literature [37]–[42]. Considerable progress in active contour segmentation were indeed made by overcoming the drawbacks of conservative forces such as eq. (3) with nonconservative alternatives, i.e. forces that cannot be expressed as gradients of a scalar potential. For example, the popular Gradient Vector Flow (GVF) method was proposed to increase robustness to noise, provide better capture range and allow active contours to progress into narrow concavities formed by objects in the image. Other similar approaches include the Generalized GVF (GGVF, [38]) and the Vector

Field Convolution (VFC). One of the most desirable properties shared by these new flow fields is their ability to preserve *perceptual boundaries* of the objects, i.e. gaps in the image that are connected visually by the human visual system [37], [38]. This can be exploited for better restoration of weak or invisible edges when applied to image enhancement with shock filters.

In the following, we propose a PDE framework for image enhancement using SF based on nonconservative edge-based force fields. Our contribution is threefold. First, the proposed Nonconservative Shock Filter scheme (NCSF) takes advantage of the recalculation of edge-based forces along the iterative process to better identify locations of shocks, yielding stable and accurate image sharpening enhancement. Secondly, we reformulate NCSF as an advection process, extending a recent work [13] to the nonconservative case and thereby enabling efficient schemes for single-channel and vector-valued image enhancement. Finally, we propose to couple the NCSF effect to anisotropic diffusion for the simultaneous denoising and sharpening of highly degraded images.

We note that the use of GVF fields as edge indicator function for shock filtering was proposed by earlier [43]. A similar idea was proposed for the suppression of mixed noise by coupling GVF-based shock filtering with a median filter [44]. A coupled anisotropic diffusion and shock filter scheme for the restoration of vector-valued images was also proposed recently [25] using generalizations of GVF to the multi-channel case [24]. However, in all these works, the field is computed prior to filtering and is not part of the filtering process, acting as a static vectorial edge map. This may be not optimal in noisy configurations where edges are ill-defined. Moreover, the relationship between advection and shock filtering is not taken into consideration.

In the next section, we describe the proposed NCSF scheme and show how a regularization method can take advantage of a dynamic use of edge flow fields along the iterative process to improve filtering results for noisy configurations.

III. PROPOSED METHOD

A. Dynamic Nonconservative Shock Filtering (NCSF)

We describe our iterative PDE scheme for image sharpening with shock filters based on nonconservative edge-based force (EBF) fields. Let $\mathcal{I}(\mathbf{x}) : \mathbf{x} \in \mathbb{R}^n \rightarrow \mathbb{R}$ be a n -dimensional image defined on a discrete grid \mathbf{x} of the image domain. Let $\mathcal{F}^t(\mathbf{x})$ be an EBF field computed dynamically at each Euler time step t of the iterative process and oriented toward edges. \mathcal{F}^t is normalized such that all vectors have unit norm. The general formulation of the proposed shock filter is:

$$\mathcal{I}_t(\mathbf{x}) = -\mathcal{P}(\mathbf{x})\|\nabla\mathcal{I}\| \quad \text{s.t.} \quad \mathcal{I}^0 = \mathcal{I}, \quad (4)$$

where $\mathcal{P}(\mathbf{x}) = \langle \mathcal{F}^t(\mathbf{x}), \hat{\nabla}\mathcal{I}(\mathbf{x}) \rangle$ is the scalar projection of \mathcal{F}^t onto the unit gradient vector $\hat{\nabla}\mathcal{I} = \nabla\mathcal{I}/\|\nabla\mathcal{I}\|$ of direction η , and $\langle \cdot, \cdot \rangle$ is the dot product.

Fig. 1 illustrates the action of the proposed shock filter on a sigmoidal signal in the 1D case. The EBF field is oriented toward the inflection point (i.e. edge in 2D/3D images). A step signal is iteratively recovered by increasing or decreasing the

signal intensity with strength $|\mathcal{P}(\mathbf{x})| \times \|\nabla\mathcal{I}\| dt$, where dt is the Euler time step.

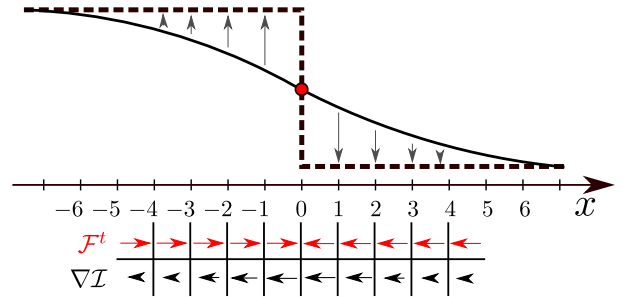


Fig. 1. Effect of the proposed NCSF on a sigmoidal 1D signal. Shocks are recovered around the inflection point at $x = 0$ (red dot) with strength proportional to $|\mathcal{P}(\mathbf{x})| \times \|\nabla\mathcal{I}\|$ (vertical arrows), where $\mathcal{P}(\mathbf{x})$ is the degree of co-alignment between \mathcal{F}^t and $\nabla\mathcal{I}$.

This formulation differs from previous GVF-based shock filtering developments [43], where the sign of the projection \mathcal{P} is used only as a replacement for the sign of the second derivative to increase or decrease signal values around the inflection point [43]. Shocks are here recovered proportionally to the degree of colinearity between the gradient direction and the EBF field. This ensures that well-defined edges, identified by the co-alignment of gradient and EBF, are enhanced with more strength. Moreover, the field is dynamically recomputed at each Euler time t , so that the estimation of the edge location is refined along the iterative process. This last property is especially useful when SF is coupled to a denoising scheme, as discussed in section III-B.

The proposed scheme implies that the EBF field \mathcal{F}^t is recomputed at each Euler step. For this reason, the use of computationally expensive flow fields such as GVF is impractical. Instead, in this work, we use Vector Field Convolution (VFC) EBF fields [40]. VFC vector fields are similar to those produced with GVF, however their computation is much faster, requiring only n convolutions in n -dimensional images, which make them well adapted to the proposed iterative approach. We briefly recall here their formulation. A VFC field is obtained by convolving a scalar edge map f^t of image \mathcal{I} at Euler time t with a *Vector Field Kernel* (VFK):

$$\mathcal{F}^t = f^t * \mathcal{K}, \quad (5)$$

where \mathcal{K} is the VFK, a vector kernel whose vectors point toward its center r_0 with decreasing magnitude $m(r) = r^{-\gamma}$ as a function of the distance r to r_0 . In this work, we set f^t as the squared Euclidean norm of the gradient $f^t = \|\nabla\mathcal{I}\|^2$.

The VFK shape is controlled by two parameters : kernel radius s and vector attenuation parameter γ . Fig. 2 shows two example VFK of size $s = 5$ with $\gamma = 2.2$ and $\gamma = 2.8$. The kernel shape is crucial to the filtering output, as it rules the detection of weak edges in the image. Using low values of γ increases robustness to noise, at the expense of smearing out weak edges which are then lost for recovery. Conversely, strong values of γ must be used to recover weak edges, at the expense of higher sensitivity to noise [40]. This is the classical conflict between edge detection and robustness to

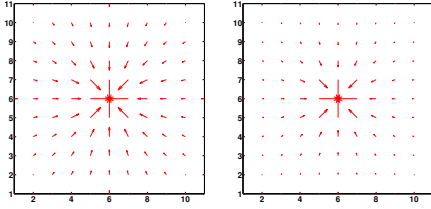


Fig. 2. VFK kernel used for VFC calculation. Vectors point toward its center r_0 with decreasing intensity. (a) $s = 5$, $\gamma = 2.2$. (b) $s = 5$, $\gamma = 2.8$. High values of γ increase sensitivity to local weak edges but also yield more sensitivity to isolated noise

noise, which are contradictory by nature [45]. This problem can be alleviated using approaches that combine both edge sharpening and denoising, which is the object of the next section.

B. Regularized NCSF for noisy images (NCRSF)

Under eq. (4), the SF acts throughout the image domain anywhere the gradient is non-zero. This includes noisy flat regions where, in principle, no sharpening should occur. It is however generally preferable to sharpen only edges while removing noise in homogeneous regions. This can be done by coupling SF to anisotropic diffusion, as originally proposed by Alvarez and Mazorra [31]. To this end, we couple the proposed EBF-based SF to a denoising approach in an Advection-Diffusion-Reaction (ADR) scheme. We use the *oriented laplacians* formalism, which decomposes anisotropic diffusion in terms of independent diffusions along the gradient and isophote directions [23].

In n -dimensional images, let η be the gradient direction and $\xi_i, i = (2, \dots, n)$ be the orthogonal directions to η that span the hyperplane tangent to the local isophote. The proposed coupled ADR scheme for simultaneous denoising and sharpening of noisy images (NCRSF for Non-Conservative Regularized Shock Filter) is expressed as:

$$\mathcal{I}_t = c_\eta(\mathcal{N})\mathcal{I}_{\eta\eta} + \sum_{i=2}^n c_{\xi_i}(\mathcal{N})\mathcal{I}_{\xi_i\xi_i} + \lambda (\mathcal{I}^0 - \mathcal{I}) - \mathcal{P}(\mathbf{x})\|\mathcal{I}_\eta\|. \quad (6)$$

The first two terms in equation (6) respectively correspond to the nonlinear diffusion of image intensities along the gradient and isophote directions, weighted by diffusion coefficients c_η and c_{ξ_i} , two decreasing functions of a scalar edge detector $\mathcal{N}(\mathbf{x})$ [20]. The third term is a *reaction* term [46], controlled by parameter λ , that helps preventing the solution from diverging too far from the initial image \mathcal{I}^0 . The last term is the proposed EBF-based SF term. In single-channel images, $\|\mathcal{I}_\eta\| = \|\nabla\mathcal{I}\|$.

In the proposed approach, the recalculation of the vector field \mathcal{F}^t at each time step enables to enhance edge detection along the process. This property is especially useful in noisy configurations where the initial edge-based field is ill-defined. The use of a static field has been considered as an advantage because it provides numerical stability [43]. However, it also

limitates the edge detection task to the accuracy of the static initial field, which can lead to erroneous sharpening of flat regions.

To illustrate the action of the proposed coupled ADR scheme, Fig. 3 shows a 100×100 grayscale image representing 4 disks of variable contrast (Fig. 3a) blurred with a Gaussian filter of scale $\sigma_b = 3$ pixels and corrupted with additive white Gaussian noise (AWGN) of standard deviation $\sigma = 10$ (Fig. 3b). The second row compares the EBF field computed on the noisy image and the one obtained with the proposed scheme after 150 iterations. The advantage of recomputing the field is emphasized on the lower contrast disks for which the gradient signal is weak. Because initial EBF vectors are almost random (Fig. 3c), enhancement approaches that rely on this noisy information [43] would perform poorly. On the contrary, the recalculation of the field using the proposed scheme produced more coherent orientations of the EBF vectors for all four disks (Fig. 3d). This can be assessed quantitatively by comparing the angular difference between EBF vectors obtained on the noise-free image and the ones obtained after processing. We define the pixelwise angular error D of an EBF vector \mathcal{F} to some reference ground-truth EBF field \mathcal{F}^0 as:

$$D(\mathcal{F}^0, \mathcal{F}) := \cos^{-1} \left(\frac{\langle \mathcal{F}^0, \mathcal{F} \rangle}{\|\mathcal{F}^0\| \|\mathcal{F}\|} \right). \quad (7)$$

By analogy with a metric proposed for color constancy assessment [47], we define an estimator of EBF field quality as the median value of the angular error distribution. We call this full-reference measure *median angular error* (MAE). Fig. 4 shows the reduction of MAE along iterations for different noise values in the *disks* image of Fig. 3. While the MAE logically increases with the standard deviation of noise, it diminishes along iterations due to the re-evaluation of the EBF

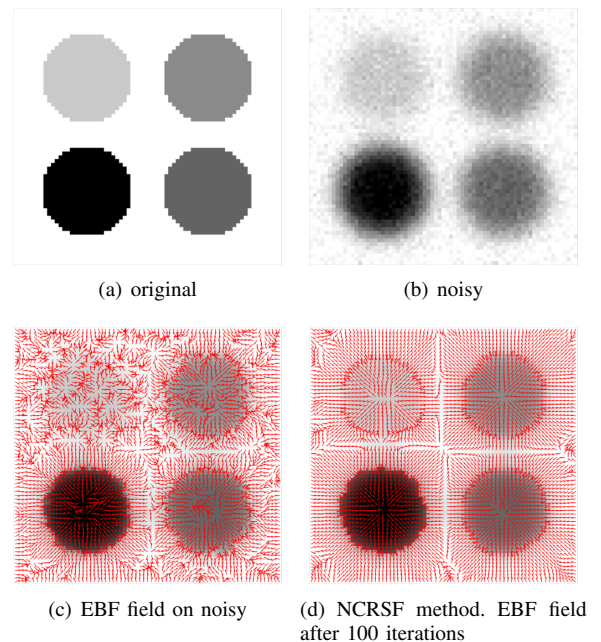


Fig. 3. Shock filter action on a synthetic *disks* image corrupted with Gaussian blur and AWGN noise

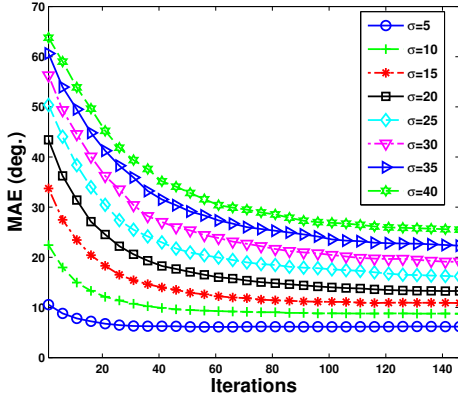


Fig. 4. Median Angular Error of EBF field \mathcal{F}^t vs. iteration time for different noise values σ in the *disks* image of Fig. 3.

field on the less noisy processed image. Thanks to the use of VFC, the computational overload of such recalculation is moderate. As an example, in this image, 150 iterations of a finite-difference scheme implementation of the approach take 0.32s, against 0.21s without recalculation of the field on a 3 GHz Intel i7 processor.

C. Extension to vector-valued images

Vector-valued (VV) images such as color, multispectral or hyperspectral images can be enhanced with the proposed scheme by processing each of their channel independently, i.e. using a marginal approach. However, it is generally preferable to couple channel evolution, e.g. to reduce the production of false colors in color images, due to unbalanced enhancement between channels [23], [48]. In the VV case, the gradient direction η and its corresponding amplitude $\|\mathcal{I}_\eta\|$ are not well defined. Simple averaging of the gradient in the channels is not satisfying, as opposite gradient directions in two channels would cancel each other without meaning [48].

To avoid this effect, the multi-channel case is handled using the *local structure tensor* (ST) formalism [49]. The ST, also known as the *second-order moment matrix*, or *Di Zenzo matrix* is a symmetric and positive semidefinite n -by- n matrix. For p -channel images, it is expressed as the sum of the covariance matrices of the gradient in the different channels :

$$J_\rho = G_\rho * \sum_{k=1}^p \nabla \mathcal{I}^k (\nabla \mathcal{I}^k)^T, \quad (8)$$

where \mathcal{I}^k denotes the k -th channel of \mathcal{I} , \cdot^T is the transposition operator and G_ρ is a regularizing Gaussian kernel of scale ρ . We follow Di Zenzo's analysis [49], where the gradient of a VV image, or *vector gradient*, is obtained from the eigendecomposition of the ST. The vector gradient direction η is the direction of the eigenvector associated with the principal eigenvalue, while the remaining eigenvectors (ξ_2, \dots, ξ_n) span the hyperplane tangent to the local isophote. The vector gradient magnitude is obtained by combining the eigenvalues of the ST [18]. In this work, we use the trace of the tensor as an edge detector as proposed in previous works

for color image enhancement [21] :

$$\mathcal{N}_V = \sqrt{\text{Tr}(J_\rho)} \quad (9)$$

We obtain a VFC field for VV images \mathcal{F}_V by convolving the squared contrast \mathcal{N}_V^2 with a vector field kernel, as proposed in the context of image segmentation [50]. Similarly to the scalar case, the proposed ADR scheme is achieved by coupling the evolution of each channel \mathcal{I}^k under:

$$\begin{aligned} \mathcal{I}_t^k = & c_\eta(\mathcal{N}_V) \mathcal{I}_{\eta\eta}^k + \sum_{i=2}^n c_\xi(\mathcal{N}_V) \mathcal{I}_{\xi_i \xi_i}^k \\ & + \lambda \left(\mathcal{I}^{k,0} - \mathcal{I}^k \right) - \mathcal{P}_V(\mathbf{x}) \|\mathcal{I}_\eta^k\|, \end{aligned} \quad (10)$$

where \mathcal{P}_V is the projection of \mathcal{F}_V^t onto the unit vector gradient direction η :

$$\mathcal{P}_V = \langle \mathcal{F}_V^t, \mathcal{I}_\eta^k / \|\mathcal{I}_\eta^k\| \rangle. \quad (11)$$

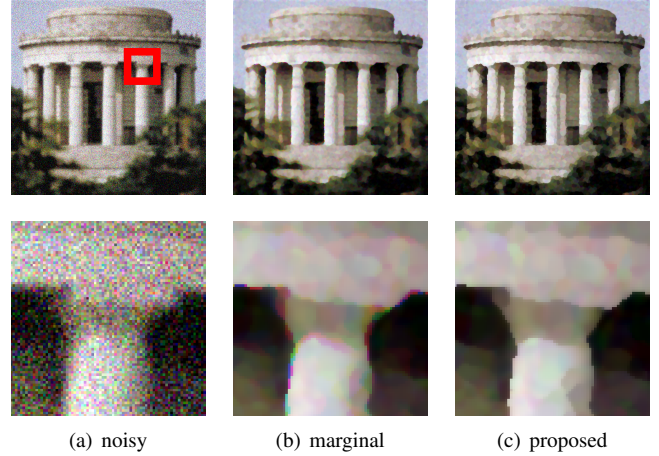


Fig. 5. Top row: processing result using the proposed NCRSF scheme on a color image corrupted by Gaussian blur and AWGN. Bottom row: magnified region marked in red. (b) Independent sharpening of each channel produces false colors at the location of shocks. (c) Coupled sharpening using the structure tensor-based EBF field restores sharpness without producing false colors. Better viewed in electronic version.

Fig. 5 illustrates the effect of the proposed ADR filtering for VV images on the 512×512 *monument* color image of the CSIQ database [51]. The clean image was blurred with a Gaussian filter of scale 2 pixels and corrupted with zero-mean AWGN of standard deviation $\sigma_n = 35$. When channels are processed independently (Fig. 5b), false colors appear around locations of shocks. Under the proposed coupled VV scheme (fig 5c), noise is suppressed efficiently without producing false colors.

D. Relationship with advection

As noted recently by Prada and Kazhdan [13], if the signed edge response is $\mathcal{L}(\mathcal{I}) = \frac{(\nabla \mathcal{I})^T H \nabla \mathcal{I}}{\|\nabla \mathcal{I}\|}$, where H is the Hessian, the classical shock filter can be expressed as:

$$\mathcal{I}_t = -\frac{1}{2} \langle \nabla \|\nabla \mathcal{I}\|^2, \nabla \mathcal{I} \rangle, \quad (12)$$

which describes the advection of image \mathcal{I} along the vector field $\frac{1}{2} \nabla \|\nabla \mathcal{I}\|^2$.

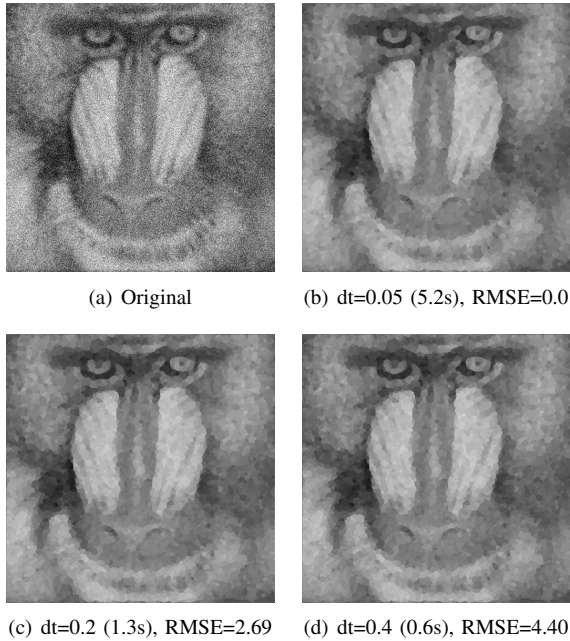


Fig. 6. Approximation of NCSF filtering for the 512×512 *mandrill* image for different values of Euler time step dt (CPU time in brackets). Image values are advected along the flow lines of the VFC field $\mathcal{F}^t dt$. Processed images with coarse time steps are hard to distinguish visually from reference $dt = 0.05$

Similarly, we approximate EBF-based shock filtering by advecting the values of \mathcal{I} for any Euler time $t + dt$ along the flow lines of the vector field \mathcal{F}^t . Due to the fact that the EBF field is smooth and well aligned in homogeneous regions, such advection will also lead to the denoising of non-edge pixels. Fig. 6 shows the effect of the proposed advection scheme on the *mandrill* grayscale image for various time steps dt at fixed Euler time $t = 6.4$. For all step values, the image was denoised and its edges were sharpened, showing mild increase of the root mean square error (RMSE) for larger steps when compared to the arbitrary reference result obtained with $dt = 0.05$.

IV. VALIDATION SETUP

The evaluation of image enhancement is generally subjective or, if used as a pre-processing stage, specific to the task at hand [11]. This is in contrast with image restoration, which can be assessed quantitatively using full-reference image quality metrics such as signal-to-noise ratio (SNR) or root mean square error (RMSE) [12]. Although the maximization of such quantities is not a primary objective, there is in general some overlap between the effects of restoration and enhancement (e.g. both may denoise the image). Full-reference metrics can therefore be used in conjunction with application-specific evaluation to assess the effect of the proposed approach. Provided the targeted application can be evaluated objectively using image quality metrics, the relative improvement of these metrics due to pre-processing can also indirectly assess the interest of the method.

In the next section, we show how our approach can facilitate several tasks such as image restoration, edge detection, image

sharpening or segmentation in various imaging contexts. We describe in the following the datasets and the associated quantitative evaluation metrics that we used in our experiments.

We start by studying the effect of the filter on a noisy one-dimensional signal. We then investigate the value of our approach in two different types of medical images. First, we consider the enhancement of TRUS images with the aim of facilitating automatic contour-based prostate segmentation. We then focus on the enhancement of partial volume corrected brain PET images. Although the proposed NCRSF approach is not specifically tailored for image restoration, it can perform satisfyingly in this regard on heavily distorted images. Additional results in the context of natural image restoration using NCRSF on images corrupted by heavy noise and blur can be found in the supplemental material of this article, alongside comparisons with other restoration approaches.

A. One-dimensional case

We studied the simplified and controlled scenario of a one-dimensional sigmoidal signal degraded by heavy additive white Gaussian noise (AWGN). The Matlab code necessary to reproduce the results of this section was released online¹.

1) *Signal description*: The studied sigmoid $S(t)$ is expressed as:

$$S(t) = \frac{1}{\pi} \arctan \left[4\pi \left(t - \frac{1}{2} \right) \right] + \frac{1}{2}. \quad (13)$$

An additive white Gaussian noise of variance $\sigma_n = 0.4^2$ was added to $S(t)$. Our objective was to recover a step signal around the inflection point at $t = 1/2$. We limited our study to the interval $[-\frac{1}{2}, \frac{3}{2}]$, and discretized the signal into 10^3 samples (Fig. 8a).

2) *Comparative evaluation*: In this 1D example, we compared the proposed NCRSF filter to the Coupled Complex Diffusion and Shock Filtering (CDSF) scheme of Gilboa, Sochen and Zeevi [32]. CDSF is, like NCRSF, a PDE-based approach that couples anisotropic diffusion and regularized shock filter and is arguably the work closest to ours in its formulation. It is based on complex diffusion [33], where the diffusion in the gradient direction and shock filtering strength are controlled by a time-dependent complex parameter λ . The real part of λ decreases with Euler time in order to progressively reduce diffusion in the gradient direction and increase shock filter strength along iterations. We set the parameters of both CDSF and NCRSF models so as to maximize the SNR between the filtered signal and the idealized step edge.

3) *Quantitative metrics*: We studied three objective quantitative metrics. The SNR with respect to the idealized step signal was used to assess restoration. The maximum gradient amplitude $\|\nabla S\|_{\max}$ was used to evaluate sharpness recovery. Finally, the total variation TV was considered to evaluate the piecewise constantness of the output. The TV is defined as:

$$\text{TV} = \int_{-\frac{1}{2}}^{\frac{3}{2}} |\partial_t S(t)| dt \quad (14)$$

and is equal to 1 for the true step signal.

¹<http://stockage.univ-brest.fr/~vjaouen/tip2018/>

B. Enhancement of TRUS images

1) *Dataset description:* TRUS imaging is largely employed for the evaluation of prostate diseases and plays an important role in most prostate therapy setups such as high intensity focus therapy or brachytherapy. Although TRUS has many advantages such as real-time capability and low cost, the produced images suffer from important limitations.

Ultrasound images (US) are affected by various degradations including low contrast, blur and speckle noise, making the accurate identification of anatomical structures difficult. To increase SNR, most US-dedicated image filters take into account the multiplicative nature of speckle noise in their formulation [26]. Similar noise statistics can be found in other domains such as optical coherence tomography or radar imaging, with related efforts to tackle this issue [52]–[54]. Speckle noise is however not the only difficulty encountered in TRUS imaging. Depending on probe quality, acquisition parameters and, to a lesser extent, patient anatomy, the gland volume can be difficult to segment automatically. One of the most problematic degradation is the weakness of the prostate boundaries, a problem that cannot be addressed only through denoising (i.e. in the present case, despeckling). For this reason, automatic segmentation of the prostate is a very challenging task even for state of the art techniques [55], [56]. The consensus in the prostate segmentation community is therefore that edge information alone is not sufficient to perform accurate prostate segmentation [57].

To remain generic and widely applicable, the proposed NCRSF approach is not specifically tailored to address the multiplicative nature of the noise. Nevertheless, we show in the remainder of this section that such a method can be effective for improving prostate segmentation and edge detection in TRUS.

In our experiments, we used a set of 14 images from patients with prostate cancer obtained before undergoing prostate brachytherapy treatment at the Brest University Hospital, Brest, France. For all images, contours of the gland were manually delineated in all slices by an expert radiation oncologist to provide reference results for edge detection and segmentation experiments.

2) *Comparative evaluation:* PDEs are popular among the ultrasound imaging community for facilitating edge detection and segmentation [26]. One of the reasons for this popularity is their ability to explicitly adapt the filtering effect to the characteristics of speckle noise. The Speckle Reducing Anisotropic Diffusion (SRAD) [58], where the scalar diffusion coefficient is controlled in a nonlinear way by the local coefficient of variation, was proposed to address this issue. This can be considered as the generalization of the isotropic Lee filter to the nonlinear case [59]. A truly anisotropic variant of SRAD (i.e. not only nonlinear), *oriented SRAD* (OSRAD) using a matrix-based formulation which decouples diffusion along the gradient and isophote directions was proposed [60]. In a comprehensive comparative study between despeckling filters [26], OSRAD was shown to perform better than SRAD. Recently, a new matrix-based anisotropic diffusion equation coupled to a delay differential equation [29] using an adaptive Volterra-type

memory mechanism [61] based on speckle statistics (ADMSS) to better preserve relevant structural information in medical images was proposed, obtaining better results than OSRAD. In our experiments, we compared our NCRSF approach to SRAD and ADMSS using the implementation provided by the authors^{2,3}. While the objective of this section is to compare the effects of local PDE filters, we also include quantitative results obtained using SAR-BM3D⁴ [62], a popular adaptation of the BM3D patch-based denoising method [2] to speckle noise that generally performs satisfyingly in speckle ultrasound images [63].

3) *Quantitative metrics:* We evaluated the proposed approach using metrics commonly found in ultrasound imaging for image quality assessment [26]: Pratt's Figure Of Merit (PFOM) [64], Structural similarity (SSIM) [65], Contrast-to-noise ratio (CNR), as well as a more recent metric for sharpness assessment, the S_2 sharpness score [66].

Given two binary edge maps X and Y , where Y is the ground truth, the PFOM returns a number between 0 and 1 that measures the similarity between edges, both in terms of detection and pixel displacement. It is defined as:

$$\text{PFOM}(X, Y) = \frac{1}{\max(N_X, N_Y)} \sum_{i=1}^{N_X} \frac{1}{1 + \alpha d_i^2}, \quad (15)$$

where N_X and N_Y are respectively the number of detected and actual edge pixels, d_i denotes the distance from the i th-detected edge pixel to the nearest actual edge and α is a scaling constant set to $1/9$. Edge maps were obtained by binarizing the gradient magnitude maps above the 95th percentile, which corresponds to the average percentage of pixels belonging to the prostate boundaries in the ground truth images. While the Canny filter is often used for PFOM [26], scores were considerably better in our dataset with this simple thresholding, regardless of the method used.

The SSIM measure is defined as:

$$\text{SSIM}(X, Y) = \frac{(2\mu_1\mu_2 + C_1)(2\sigma_{12} + C_2)}{(\mu_1^2 + \mu_2^2 + C_1)(\sigma_1^2 + \sigma_2^2 + C_2)} \quad (16)$$

where μ_1, μ_2 are local means of reference and test images, σ_1, σ_2 are the corresponding local standard deviations and σ_{12} is the covariance between X and Y . Constants C_1 and C_2 are set as specified in the Matlab r2016a implementation of the metric. As it is often the case for clinical image evaluation, no distortion-free ground truth images were available. The reference image used for SSIM was the original unprocessed image as proposed in previous studies [26]. In this case, the SSIM score provides an indication of to what extent original structures were preserved with respect to the noisy input and thus cannot be considered as an image restoration metric.

The CNR is defined as :

$$\text{CNR} = \frac{|\mu_1 - \mu_2|}{\sqrt{\sigma_1^2 + \sigma_2^2}}, \quad (17)$$

where μ_1 and σ_1^2 are the mean and variance of a small region of interest and μ_2 and σ_2^2 are the mean and variance of a

²<https://sites.google.com/site/gramoslorden/admss>

³<http://viva-lab.ece.virginia.edu/downloads.html>

⁴ <http://www.grip.unina.it/research/80-sar-despeckling/>

homogeneous region of similar dimensions in the background. In the ultrasound image dataset, we selected small rectangular regions of approximately 5 mm^2 (or 15×15 pixels) in the background and in the foreground.

The S_2 spatial sharpness score is a total variation-based metric for natural image sharpness assessment. For an image scaled between 0 and 1, the local total variation (LTV) $v(\mathbf{x})$ of each pixel \mathbf{x} is first computed as:

$$v(\mathbf{x}) = \frac{1}{4} \sum_{i,j} |x_i - x_j|, \quad (18)$$

where the absolute difference is taken between all the pixels in a 2×2 local patch at \mathbf{x} . Since blurred image edges tend to have a low LTV, the maximum value of $v(\mathbf{x})$ in $b \times b$ overlapping superblocks, with $b > 2$, gives a spatial map of the local sharpness of an image at scale b . The S_2 index is obtained by averaging the 1% highest pixel values of the spatial map.

To further attest the performance of the proposed method for edge detection in ultrasound images in a segmentation context, we segmented the prostate gland using an edge-based level set active contour. We compared our segmentation results to those obtained on raw images, SRAD-filtered and ADMSS-filtered images. The active contour model used in our experiments is briefly described in the next lines.

Let $\mathcal{C}(t)$ be an active contour defined as the zero level-set of a 2D function $\phi(\mathbf{x}, t)$ defined across the image domain. The evolution equation of ϕ according to curvature motion and edge-based external forces is expressed as:

$$\phi_t(\mathbf{x}) = \alpha [\kappa(x) |\nabla \phi(\mathbf{x})|] - \beta [\mathcal{F}_{\text{edge}}(\mathbf{x}) \cdot \nabla \phi(\mathbf{x})], \quad (19)$$

where κ is the curvature of ϕ , $\mathcal{F}_{\text{edge}}$ is an EBF field and α, β are parameters that control the respective strengths of curvature motion and edge-based forces. The EBF field $\mathcal{F}_{\text{edge}}$ is a VFC field based on the squared image gradient magnitude. Images were prepared by centering and cropping the field of view around the prostate. For all methods and all images, we initialized $\mathcal{C}(t=0)$ to a rectangle centered around the prostate and at equal distance of the image boundaries (dotted white contour in Fig. 11). We then let the contour evolve according to eq. (19) by considering equal parameters for all tested images and compared the segmentation result (Fig. 11, in yellow) to its ground truth (Fig. 11, in red) using the Jaccard similarity coefficient [67] and the Mean Absolute Distance (MAD), which expresses the average distance between the segmented surface and ground truth [68]. Active contour parameters (number of iterations, α , β , VFK kernel shape) and filter parameters were optimized so as to produce the best average Jaccard score for the tested method on a training dataset of 3 additional TRUS images not included in our evaluation dataset.

C. Enhancement of partial volume corrected PET images

We also performed experiments on partial-volume corrected brain PET images. Because of the scanner point spread function (PSF) of limited spatial resolution and several intrinsic physical factors, PET images suffer from partial volume effects (PVE). PVE are responsible for blur and fuzzy transitions between areas of different radiotracer uptakes, as well as

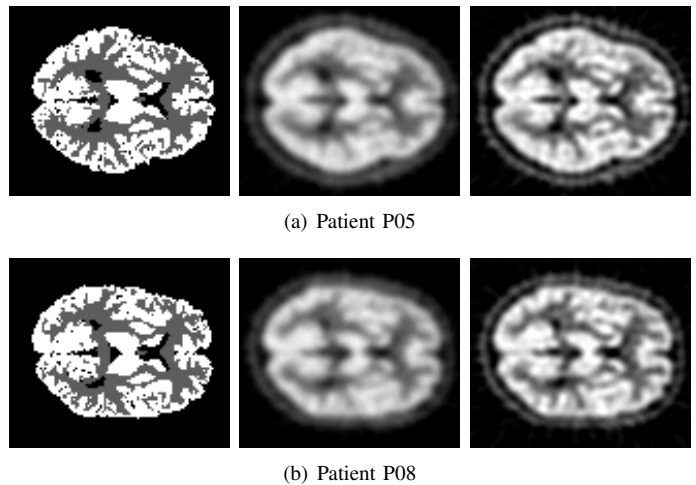


Fig. 7. Example transaxial PET slices in patients P05 and P08 of the PET-SORTEO database. Left: ground truth reference. Middle: original PET image. Right: partial volume correction with RVC.

inaccurate quantification (under or over estimation) due to spill-in and spill-out effects [69]. It is generally required to correct for PVE prior to analyzing PET data, a process known as partial volume correction (PVC) [70]. PVC is especially useful in quantitative analysis, as uncorrected PET images may lead to standardized uptake values of poor clinical interpretability [69]. This is however a difficult and ill-posed problem, and most state of the art PVC methods rely on accurate segmentation of co-registered anatomical data obtained from modalities such as MRI or CT [71], [72]. These methods rely on the strong assumption that PET functional regions and anatomical regions coincide. If this assumption cannot be made, or in the absence of availability of accurate co-segmentation of anatomical data, deconvolution approaches like the Richardson-Lucy and the reblurred Van Cittert algorithms are typically considered [73]. While alleviating the need for anatomical information, these methods are however less efficient at PVC than anatomical-based methods, as they amplify image noise [74], [75] and are generally not capable of fully recovering image sharpness [70]. In the following, we show how the proposed NCSF shock filtering scheme can be employed to enhance deconvolution-based PVC results.

1) *Image description:* We evaluated our approach using the PET-SORTEO database [76]. PET-SORTEO is an open database of highly realistic Monte Carlo simulations of labelled brain PET images that aims at providing reliable ground truth for the validation of PET-dedicated algorithms. The database contains 15 patient brain PET simulated images derived from actual magnetic resonance scans. In our experiments, we focus on the static ^{18}F -FDG study, showing two functional regions corresponding to differences in uptake of ^{18}F -FDG between cortical gray matter and white matter (Fig. 7, first column). These images were reconstructed into $128 \times 128 \times 63$ voxels using a filtered back-projection algorithm, leading to high PVE throughout the field of view and relatively low noise levels (Fig. 7, second column).

A partial-volume corrected PET image (the input of the

proposed NCSF approach) was obtained using the Reblurred Van Cittert (RVC) algorithm. RVC is an iterative approach that seeks a solution, in the least squares sense, to the following minimization problem:

$$\|I_b - H * \tilde{I}\|, \quad (20)$$

where I_b is the blurred image, \tilde{I} is the deconvolved image and H is a blur kernel (usually Gaussian), whose PSF is assumed to be known and spatially invariant.

An estimate of \tilde{I} is obtained by the following iterative scheme:

$$\tilde{I}_{k+1} = \tilde{I}_k + \alpha \left(H * (I_b - H * \tilde{I}_k) \right), \quad (21)$$

where \tilde{I}_k is the corrected image after k iterations and α is a step parameter, usually set around 1.5 [77]. RVC parameters were set so as to minimize the mean square error with respect to the ground truth image. The parameters obtained ($\alpha = 1.5$; Gaussian PSF of full width at half maximum $9.1 \times 9.1 \times 9.3$ mm³) were found to be in agreement with values reported in a previous PET-SORTEO study for another tracer, using a different optimization strategy [77]. The last column of Fig. 7 shows the RVC outputs corresponding to these two patients. While contrast is increased, functional boundaries remain substantially blurred and noise levels are amplified.

Our objective was to show that NCSF can enhance the quality of the RVC-based partial volume corrected output. In this experiment, NCSF parameters were set equally for all images and optimized so as to maximize on average the SSIM with respect to the ground truth reference.

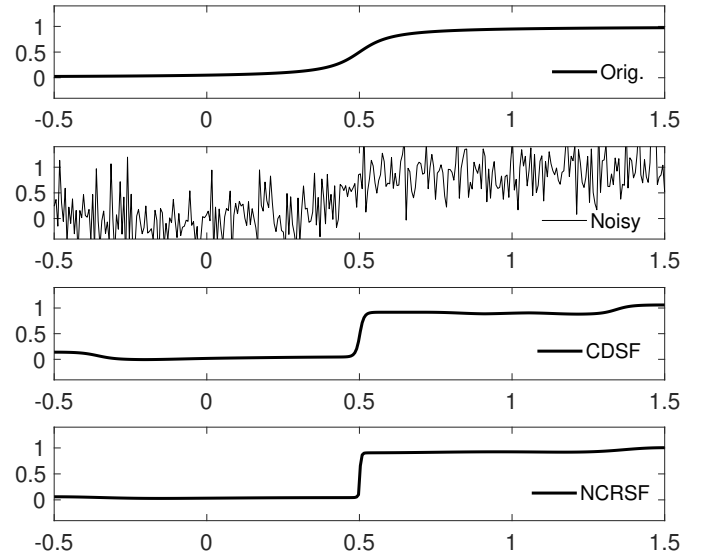
2) *Quantitative metrics*: Alongside SSIM, we quantified PET image enhancement using application-specific metrics. A parameter of interest in PET quantification is the gray to white-matter activity ratio R , equal to 2.72 in the ground truth images. R was determined for each image by averaging activity within the two ground truth labelled regions. Sharpness recovery was assessed by the average gradient magnitude inside the brain $\|\nabla I\|_{\max}$ and by the S_2 index.

V. RESULTS

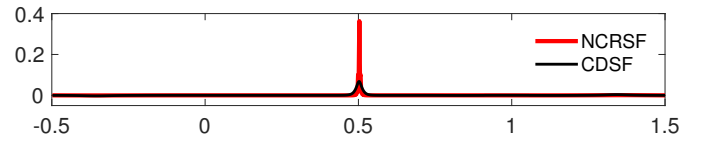
A. One-dimensional signal

Fig. 8a compares the effect of CDSF and NCRSF on the one-dimensional sigmoidal signal $S(t)$. Corresponding quantitative metrics are provided in Table I. Note that the TV of the clean sigmoid is not exactly 1 due to the interval restriction. While both methods successfully denoise the signal, NCRSF was better at recovering the step edge around the inflection point at $t = 1/2$. This result is highlighted in Fig. 8b that shows the corresponding gradient amplitude of CDSF and NCRSF, with a maximum gradient amplitude about 5 times higher in the case of NCRSF at the inflection point (0.36 for NCRSF against 0.07 for CVDS). The signal was significantly flatter far from the edge with most gradient energy concentrated near the step edge. The TV was also closer to unity (NCRSF: TV= 1.02, CVDS: TV= 1.32), showing fewer spurious gradient signal within the flat regions.

A likely explanation for the better performance of NCRSF is that both shock filtering and diffusion are acting on the signal,



(a) From top to bottom: Clean sigmoid, Noisy sigmoid, CDSF [33] and proposed NCRSF.



(b) Gradient amplitudes for CDSF and NCRSF. Maximum gradient amplitude near the step edge is more than 5 times higher for NCRSF.

Fig. 8. Recovery of a step signal from a noisy sigmoid in the 1D case.

TABLE I
QUANTITATIVE SCORES FOR THE 1D SIGNAL

	SNR	TV	$\ \nabla S\ _{\max}$
Step signal	∞	1	1
Clean sigmoid	14.7	0.95	0.008
Noisy sigmoid	4.5	441.55	1.828
CDSF	18.42	1.32	0.068
NCRSF	20.64	1.02	0.363

regardless of the iteration time. In CDSF, shock filtering is gradually increased with Euler time but the process starts with a purely diffusive process that smears out the edge excessively. A smaller initial diffusion strength for CDSF would lead to a noisier estimation of the inflection point, and consequently irreversible spurious sharpening of the two flat regions. The intrinsic regularization of the inflection point localization with NCRSF helps overcoming this effect.

In the following, we show results in the more complex context of multidimensional medical images.

B. Ultrasound images

Fig. 9 shows filtering results for SRAD, ADMSS and NCRSF in two transaxial B-mode TRUS images of our clinical dataset (first and third columns). The prostate can be globally described as an hypoechoic medium, showing as a dark, "walnut-shaped" region surrounded by a brighter, more echoic medium. The dots appearing in the unprocessed and SRAD images correspond to artificial grid points superimposed onto the original image. All filters showed substantial denoising

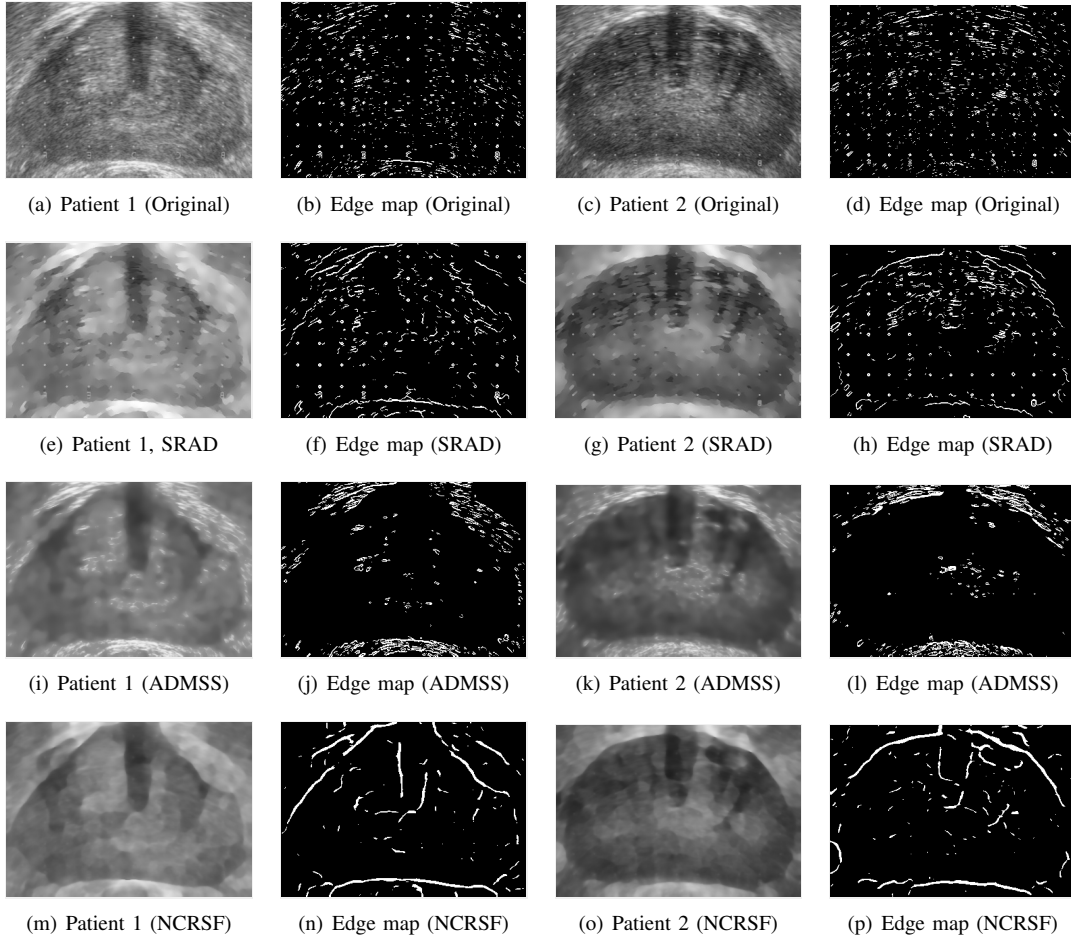


Fig. 9. Example processing results for axial TRUS images of two patients of our clinical dataset and corresponding edge maps. From top to bottom: clinical image, SRAD [58], ADMSS [29] and proposed NCRSF filter.

capability with different properties. ADMSS tended to better preserve the aspect of the original image, including the smoothness of its edges. The ADMSS filtered images also preserved textural information irrelevant for the contour-based segmentation, showing heterogeneous features throughout the gland due to calcifications. Both SRAD and NCRSF showed better edge-enhancing properties, with a better contrast between background and foreground for NCRSF, alongside with stronger denoising and flattening of the gland. The better behavior of NCRSF for prostate edge detection is stressed on the binary edge maps obtained using an automatic gradient-based edge detector (second and fourth columns). Edges coincide more clearly with the prostate boundaries, with less spurious gradients owing to noise or smaller artifacts. Fig. 10 shows the corresponding S_2 sharpness maps of the images from the first column of Fig. 9. Because the S_2 score is sensitive to noise, the original image shows high sharpness values throughout the field of view. This measure is indeed sensitive to noise, due to global increase of total variation in noisy images. Nevertheless, we find the visualization of sharpness maps useful even in noisy images, where they provide an easy qualitative understanding of which image regions show strong edges, consistently with the sharpness

perceived by the observer. In the NCRSF-filtered image, sharp regions mostly coincide with true prostate edges, contrarily to SRAD or ADMSS. Still, some edges belonging to the prostate could not be recovered in difficult regions for which no gradient was detected.

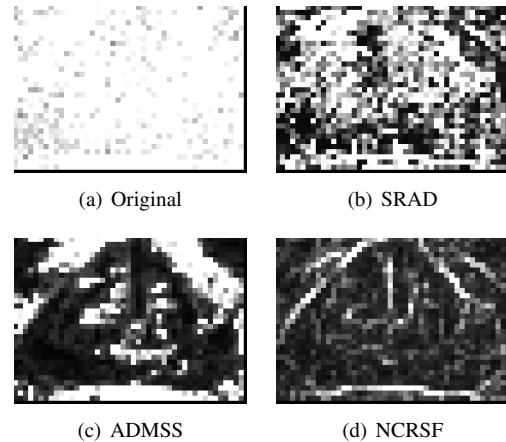


Fig. 10. Effect of the filtering on perceived image sharpness in a TRUS image using TV-based S^2 sharpness map with block size 8 [66]. NCRSF sharpened regions mainly coincide with true prostate edges.

TABLE II
QUANTITATIVE SCORES FOR THE TRUS IMAGE DATASET ($n = 14$)

	SSIM	PFOM	CNR
Noisy	1	0.13 ± 0.02	0.91 ± 0.62
SRAD	0.39 ± 0.03	0.17 ± 0.03	1.26 ± 0.85
ADMSS	0.47 ± 0.08	0.18 ± 0.05	1.16 ± 0.88
SAR-BM3D	0.75 ± 0.04	0.16 ± 0.03	1.02 ± 0.70
NCRSF	0.30 ± 0.02	0.27 ± 0.05	1.41 ± 0.99

These visual observations are further attested by the quantitative metrics calculated on the 14 TRUS images of the dataset shown in Table II. The better similarity between the ADMSS output and the original image is confirmed, showing a higher SSIM score. SAR-BM3D altered the least the original unprocessed image, with a SSIM score of 0.75 ± 0.04 on average, at the expense of lower edge detection capability and contrast recovery. Both PFOM and CNR values were higher when using NCRSF, consistently with higher edge detection accuracy. This suggests that edge-based segmentation of the prostate can be facilitated by prefiltering images using the proposed approach.

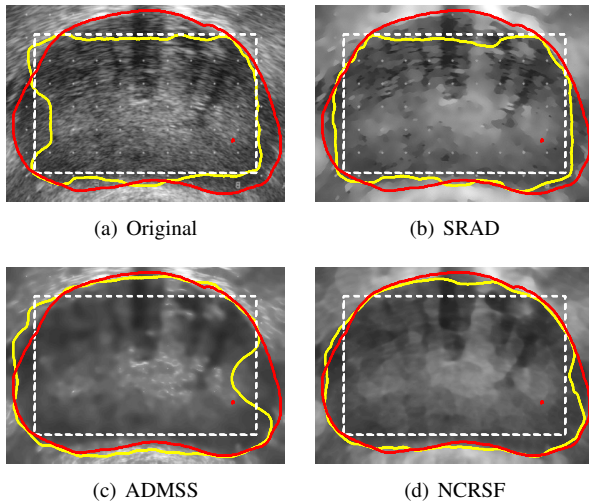
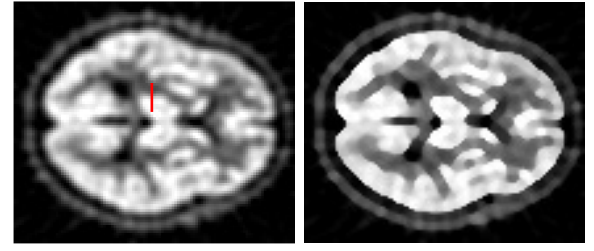


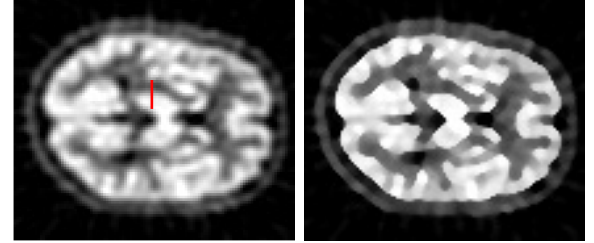
Fig. 11. Effect of the coupled ADR scheme on active contour segmentation of the prostate. Initial state is in dotted white, manual ground truth in red, segmentation result in yellow.

To support this statement, Table III shows the Jaccard and MAD segmentation results obtained using unprocessed, SRAD-, ADMSS-, SAR-BM3D- and NCRSF-filtered images. Segmentation metrics were higher (increased Jaccard values and smaller MAD) when NCRSF was used as a pre-processing stage, which is consistent with the edge detection results obtained. While being very efficient at denoising and having some edge-enhancing properties due to inverse diffusion behavior around edges [58], despeckling filters such as SRAD, ADMSS cannot make the edges sufficiently sharp to yield satisfying segmentation results with edge-based approaches.

Image edges are often deemed unuseable in the TRUS segmentation literature, and region-based approaches based on image statistics are often preferred [26]. However, results obtained with the proposed NCRSF scheme suggest that edge information can be exploited to obtain meaningful segmenta-



(a) Patient P05



(b) Patient P08

Fig. 12. Example enhancement of deconvolution-based partial volume correction results for patient P05 and P08 of the PET-SORTEO database. Left: RVC only. Right: RVC+NCSF.

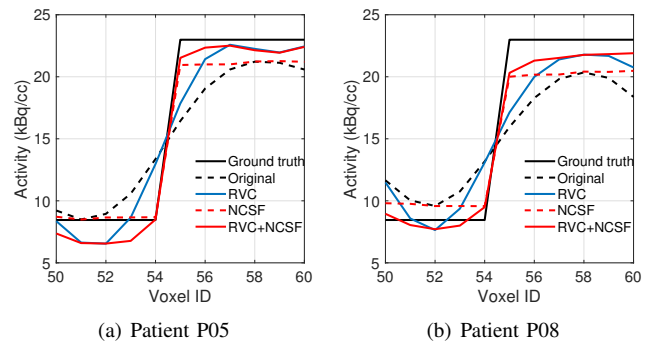
tion results provided the image is appropriately pre-processed.

TABLE III
SEGMENTATION SCORES FOR THE TRUS IMAGE DATASET ($n = 14$)

	Jaccard	MAD (mm.)
Original	0.72 ± 0.06	2.89 ± 0.60
SRAD	0.77 ± 0.09	2.43 ± 0.88
ADMSS	0.77 ± 0.11	2.32 ± 1.17
SAR-BM3D	0.75 ± 0.07	2.63 ± 0.71
NCRSF	0.85 ± 0.05	1.54 ± 0.53

C. Partial volume corrected brain PET images

Partial volume corrected images of the PET-SORTEO database were processed using the proposed NCSF shock filtering scheme, referred to as RVC+NCSF in the following. For these 3D images, computation time was about 25 seconds on average on a Core i7 CPU using 45 iterations of an explicit finite difference scheme.



(a) Patient P05

(b) Patient P08

Fig. 13. Activity profiles across the left thalamic nucleus for patients P05 and P08 along the line overlaid in Fig. 12.

Fig. 12 shows representative filtering results in transaxial PET slices for patients P05 and P08. From visual inspection, RVC+NCSF images were significantly sharper than RVC alone, showing more acute functional boundaries between gray and white matter. Fig. 13 further supports this statement by comparing one-dimensional profiles in the vicinity of the left thalamic nucleus along the line overlaid in the first column of Fig. 12. Ground truth, RVC and original profiles are also shown, as well as results obtained by applying NCSF directly to the original PET image. Whereas RVC partially recovered lost activity and increased image contrast, it was not able to form a step edge at the thalamic boundary and images remained significantly blurred. NCSF being a total variation preserving filter, it did not change the extremal values of the original PET image. Nevertheless, it significantly increased image sharpness by fully recovering a step edge at the thalamus boundary, similarly to 1D results presented in section V-A. RVC+NCSF, by taking advantage of the deconvolution of RVC, better recovered the gray to white matter activity contrast while taking advantage of the proposed shock filter to obtain a sharp functional boundary of one voxel width.

Average quantitative results obtained across the entire dataset are presented in Table IV and confirm these qualitative observations. The SSIM score showed an increase of 15% on average when compared to RVC (0.186 ± 0.005 against 0.162 ± 0.004), suggesting additional image restoration capability. The perceived sharpness was increased substantially increased, with a 72% increase of the maximum brain gradient amplitude, and a 240% increase of the S_2 score between RVC and RVC+NCSF. The gray-to-white matter activity also showed a moderate increase compared to its value in the original PET image (+11.6% for RVC against +15.2% for RVC+NCSF).

Deconvolution based partial volume correction like the Reblurred Van Cittert method are standard in PET image processing pipelines. However, they are usually not able to fully recover image sharpness and tend to amplify image noise. We showed that PET image analysis can benefit from additional post-processing using the proposed nonconservative shock filtering scheme, both visually and quantitatively. The NCSF-filtered images show stronger gradient signal between functional regions and flatter profiles within regions when compared to results obtained with RVC only.

In the PET-SORTEO database, partial volume effects (i.e. blur and quantitative bias) are the main cause of image degradation. Images show only mild levels of noise due to the strong regularization induced by the filtered back-projection reconstruction algorithm. We thus focused on the shock filtering part of the scheme (ie. NCSF and not NCRSF). However, iterative reconstructions using methods such as ordered subset expectation maximization (OSEM) are now preferred in the PET community. While yielding more accurate image quantification, they generally induce more noise in the data. In that case, a coupled regularization and shock filtering method using NCRSF would likely improve results over NCSF only.

TABLE IV
QUANTITATIVE SCORES FOR THE PET SORTEO DATABASE ($n = 15$)

	SSIM	S_2	$\ \nabla I\ _{\max}$	R
True	1.0	1.0	18.46 ± 1.86	2.72
Orig.	0.101 ± 0.003	0.20 ± 0.00	3.99 ± 0.12	1.38 ± 0.01
RVC	0.162 ± 0.004	0.27 ± 0.01	7.17 ± 0.31	1.54 ± 0.01
RVC+NCSF	0.186 ± 0.005	0.65 ± 0.02	12.31 ± 0.42	1.59 ± 0.02

VI. CONCLUSION

We have proposed a new method for the progressive restoration of images degraded by noise and blur using shock filters. The proposed NCSF approach exploits nonconservative edge based force fields that were normally designed for segmentation. By iteratively refining edge localization, it produces images with strong discontinuities that facilitate higher level tasks such as edge detection or segmentation. NCSF is especially useful when coupled with an anisotropic diffusion framework in noisy configurations (NCRSF), as edges that are not well defined prior to filtering can be iteratively recovered. Results on various types of medical images (ultrasound and PET) were used to evaluate the performance and the genericity of the proposed enhancement approach.

ACKNOWLEDGMENT

This work was partly supported by the French ANR within the Investissements d'Avenir program (Labex CAMI) under reference ANR-11-LABX-0004 (Integrated project CAPRI).

REFERENCES

- [1] A. Buades, B. Coll, and J.-M. Morel, "A non-local algorithm for image denoising," in *Computer Vision and Pattern Recognition, 2005. CVPR 2005. IEEE Computer Society Conference on*, vol. 2. IEEE, 2005, pp. 60–65.
- [2] K. Dabov, A. Foi, V. Katkovnik, and K. Egiazarian, "Image denoising by sparse 3-D transform-domain collaborative filtering," *IEEE Transactions on Image Processing*, vol. 16, no. 8, pp. 2080–2095, 2007.
- [3] —, "BM3D image denoising with shape-adaptive principal component analysis," in *SPARS'09-Signal Processing with Adaptive Sparse Structured Representations*, 2009.
- [4] W. Dong, G. Shi, and X. Li, "Nonlocal image restoration with bilateral variance estimation: A low-rank approach," *IEEE Transactions on Image Processing*, vol. 22, no. 2, pp. 700–711, 2013.
- [5] M. Lebrun, A. Buades, and J.-M. Morel, "A nonlocal bayesian image denoising algorithm," *SIAM Journal on Imaging Sciences*, vol. 6, no. 3, pp. 1665–1688, 2013.
- [6] M. Aharon, M. Elad, and A. Bruckstein, "K-SVD: An algorithm for designing overcomplete dictionaries for sparse representation," *IEEE Transactions on signal processing*, vol. 54, no. 11, pp. 4311–4322, 2006.
- [7] J. Zhang, D. Zhao, and W. Gao, "Group-based sparse representation for image restoration," *IEEE Transactions on Image Processing*, vol. 23, no. 8, pp. 3336–3351, 2014.
- [8] A. Levin and B. Nadler, "Natural image denoising: Optimality and inherent bounds," in *Computer Vision and Pattern Recognition (CVPR), 2011 IEEE Conference on*. IEEE, 2011, pp. 2833–2840.
- [9] P. Chatterjee and P. Milanfar, "Is denoising dead?" *IEEE Transactions on Image Processing*, vol. 19, no. 4, pp. 895–911, 2010.
- [10] Y. Romano, M. Elad, and P. Milanfar, "The little engine that could: Regularization by denoising (red)," *SIAM Journal on Imaging Sciences*, vol. 10, no. 4, pp. 1804–1844, 2017.
- [11] R. C. Gonzalez and R. E. Woods, *Digital Image Processing (3rd Edition)*. Upper Saddle River, NJ, USA: Prentice-Hall, Inc., 2006.
- [12] B. Zhang and J. P. Allebach, "Adaptive bilateral filter for sharpness enhancement and noise removal," *IEEE Transactions on Image Processing*, vol. 17, no. 5, pp. 664–678, 2008.

- [13] F. Prada and M. Kazhdan, "Unconditionally stable shock filters for image and geometry processing," in *Computer Graphics Forum*, vol. 34, no. 5. Wiley Online Library, 2015, pp. 201–210.
- [14] C. R. Vogel, *Computational methods for inverse problems*. SIAM, 2002.
- [15] D. Mumford and J. Shah, "Optimal approximations by piecewise smooth functions and associated variational problems," *Communications on pure and applied mathematics*, vol. 42, no. 5, pp. 577–685, 1989.
- [16] L. I. Rudin, S. Osher, and E. Fatemi, "Nonlinear total variation based noise removal algorithms," *Physica D: Nonlinear Phenomena*, vol. 60, no. 1-4, pp. 259–268, 1992.
- [17] T. F. Chan and J. Shen, *Image processing and analysis: variational, PDE, wavelet, and stochastic methods*. SIAM, 2005.
- [18] J. Weickert, *Anisotropic diffusion in image processing*. Teubner Stuttgart, 1998, vol. 1.
- [19] Y.-L. You, W. Xu, A. Tannenbaum, and M. Kaveh, "Behavioral analysis of anisotropic diffusion in image processing," *IEEE Transactions on Image Processing*, vol. 5, no. 11, pp. 1539–1553, 1996.
- [20] P. Perona and J. Malik, "Scale-space and edge detection using anisotropic diffusion," *IEEE Transactions on Pattern Analysis and Machine Intelligence*, vol. 12, no. 7, pp. 629–639, 1990.
- [21] D. Tschumperle and R. Deriche, "Diffusion PDEs on vector-valued images," *IEEE Signal Processing Magazine*, vol. 19, no. 5, pp. 16–25, 2002.
- [22] E. Nadernejad, H. Koohi, and H. Hassanpour, "PDEs-based method for image enhancement," *Applied Mathematical Sciences*, vol. 2, no. 20, pp. 981–993, 2008.
- [23] D. Tschumperle and R. Deriche, "Vector-valued image regularization with PDEs: A common framework for different applications," *IEEE Transactions on Pattern Analysis and Machine Intelligence*, vol. 27, no. 4, pp. 506–517, 2005.
- [24] V. Jaouen, P. Gonzalez, S. Stute, D. Guilloateau, S. Chalon, I. Buvat, and C. Tauber, "Variational segmentation of vector-valued images with gradient vector flow," *IEEE Transactions on Image Processing*, vol. 23, no. 11, pp. 4773–4785, 2014.
- [25] V. Jaouen, P. Gonzalez, D. Guilloateau, I. Buvat, and C. Tauber, "4DGVF-based filtering of vector-valued images," in *Image Processing (ICIP), 2014 IEEE International Conference on*. IEEE, 2014, pp. 4592–4596.
- [26] S. Finn, M. Glavin, and E. Jones, "Echocardiographic speckle reduction comparison," *IEEE transactions on ultrasonics, ferroelectrics, and frequency control*, vol. 58, no. 1, 2011.
- [27] C. Tauber, S. Stute, M. Chau, P. Spiteri, S. Chalon, D. Guilloateau, and I. Buvat, "Spatio-temporal diffusion of dynamic PET images," *Physics in medicine and biology*, vol. 56, no. 20, p. 6583, 2011.
- [28] J. Mohan, V. Krishnaveni, and Y. Guo, "A survey on the magnetic resonance image denoising methods," *Biomedical Signal Processing and Control*, vol. 9, pp. 56–69, 2014.
- [29] G. Ramos-Llordén, G. Vegas-Sánchez-Ferrero, M. Martín-Fernandez, C. Alberola-López, and S. Aja-Fernández, "Anisotropic diffusion filter with memory based on speckle statistics for ultrasound images," *IEEE Transactions on Image Processing*, vol. 24, no. 1, pp. 345–358, 2015.
- [30] S. Osher and L. I. Rudin, "Feature-oriented image enhancement using shock filters," *SIAM Journal on Numerical Analysis*, vol. 27, no. 4, pp. 919–940, 1990.
- [31] L. Alvarez and L. Mazorra, "Signal and image restoration using shock filters and anisotropic diffusion," *SIAM Journal on Numerical Analysis*, vol. 31, no. 2, pp. 590–605, 1994.
- [32] G. Gilboa, N. A. Sochen, and Y. Y. Zeevi, "Regularized shock filters and complex diffusion," in *European Conference on Computer Vision*. Springer, 2002, pp. 399–413.
- [33] G. Gilboa, N. Sochen, and Y. Y. Zeevi, "Image enhancement and denoising by complex diffusion processes," *IEEE Transactions on Pattern Analysis and Machine Intelligence*, vol. 26, no. 8, pp. 1020–1036, 2004.
- [34] J. Xiao, G. Pang, Y. Zhang, Y. Kuang, Y. Yan, and Y. Wang, "Adaptive shock filter for image super-resolution and enhancement," *Journal of Visual Communication and Image Representation*, vol. 40, pp. 168–177, 2016.
- [35] C. Duan and H. Lu, "A Novel Framework for Shock Filter Using Partial Differential Equations," *Entropy*, vol. 19, no. 4, p. 142, 2017.
- [36] M. Kass, A. Witkin, and D. Terzopoulos, "Snakes: Active contour models," *International journal of computer vision*, vol. 1, no. 4, pp. 321–331, 1988.
- [37] C. Xu and J. L. Prince, "Snakes, shapes, and gradient vector flow," *IEEE Transactions on Image Processing*, vol. 7, no. 3, pp. 359–369, 1998.
- [38] —, "Generalized gradient vector flow external forces for active contours," *Signal processing*, vol. 71, no. 2, pp. 131–139, 1998.
- [39] H. K. Park and M. J. Chung, "External force of snake: virtual electric field," *Electronics Letters*, vol. 38, no. 24, pp. 1500–1502, 2002.
- [40] B. Li and S. T. Acton, "Active contour external force using vector field convolution for image segmentation," *IEEE Transactions on Image Processing*, vol. 16, no. 8, pp. 2096–2106, 2007.
- [41] Y. Wang, C. Zhu, J. Zhang, and Y. Jian, "Convolutional virtual electric field for image segmentation using active contours," *PloS one*, vol. 9, no. 10, p. e110032, 2014.
- [42] P. Ghosh, L. Bertelli, B. Sumengen, and B. Manjunath, "A nonconservative flow field for robust variational image segmentation," *IEEE Transactions on Image Processing*, vol. 19, no. 2, pp. 478–490, 2010.
- [43] H. Yu and C.-S. Chua, "GVF-based anisotropic diffusion models," *IEEE Transactions on Image Processing*, vol. 15, no. 6, pp. 1517–1524, 2006.
- [44] O. Ghita and P. F. Whelan, "A new GVF-based image enhancement formulation for use in the presence of mixed noise," *Pattern Recognition*, vol. 43, no. 8, pp. 2646–2658, 2010.
- [45] S. T. Acton and A. C. Bovik, "Piecewise and local image models for regularized image restoration using cross-validation," *IEEE Transactions on Image Processing*, vol. 8, no. 5, pp. 652–665, 1999.
- [46] P. Kornprobst, R. Deriche, and G. Aubert, "Image coupling, restoration and enhancement via PDE's," in *Image Processing, 1997. Proceedings., International Conference on*, vol. 2. IEEE, 1997, pp. 458–461.
- [47] S. D. Hordley and G. D. Finlayson, "Re-evaluating colour constancy algorithms," in *Pattern Recognition, 2004. ICPR 2004. Proceedings of the 17th International Conference on*, vol. 1. IEEE, 2004, pp. 76–79.
- [48] T. Brox, J. Weickert, B. Burgeth, and P. Mrázek, "Nonlinear structure tensors," *Image and Vision Computing*, vol. 24, no. 1, pp. 41–55, 2006.
- [49] S. Di Zeno, "A note on the gradient of a multi-image," *Computer vision, graphics, and image processing*, vol. 33, no. 1, pp. 116–125, 1986.
- [50] V. Jaouen, P. Gonzalez, S. Stute, D. Guilloateau, I. Buvat, and C. Tauber, "Vector-based active surfaces for segmentation of dynamic PET images," in *Biomedical Imaging (ISBI), 2013 IEEE 10th International Symposium on*. IEEE, 2013, pp. 61–64.
- [51] E. C. Larson and D. M. Chandler, "Most apparent distortion: full-reference image quality assessment and the role of strategy," *Journal of Electronic Imaging*, vol. 19, no. 1, pp. 011006–011006, 2010.
- [52] J. Cheng, D. Tao, Y. Quan, D. W. K. Wong, G. C. M. Cheung, M. Akiba, and J. Liu, "Speckle reduction in 3d optical coherence tomography of retina by a-scan reconstruction," *IEEE transactions on medical imaging*, vol. 35, no. 10, pp. 2270–2279, 2016.
- [53] L. Fang, S. Li, R. P. McNabb, Q. Nie, A. N. Kuo, C. A. Toth, J. A. Izatt, and S. Farsiu, "Fast acquisition and reconstruction of optical coherence tomography images via sparse representation," *IEEE transactions on medical imaging*, vol. 32, no. 11, pp. 2034–2049, 2013.
- [54] R. Kafieh, H. Rabbani, and I. Selesnick, "Three dimensional data-driven multi scale atomic representation of optical coherence tomography," *IEEE transactions on medical imaging*, vol. 34, no. 5, pp. 1042–1062, 2015.
- [55] X. Li, C. Li, A. Fedorov, T. Kapur, and X. Yang, "Segmentation of prostate from ultrasound images using level sets on active band and intensity variation across edges," *Medical physics*, vol. 43, no. 6, pp. 3090–3103, 2016.
- [56] V. Jaouen, J. Bert, K. A. Mountris, N. Boussion, U. Schick, O. Pradier, A. Valeri, and D. Visvikis, "Prostate Volume Segmentation in TRUS using Hybrid Edge-Bhattacharyya Active Surfaces," *IEEE Transactions on Biomedical Engineering*, pp. 1–1, 2018.
- [57] S. Ghose, A. Oliver, R. Martí, X. Lladó, J. C. Vilanova, J. Freixenet, J. Mitra, D. Sidibé, and F. Meriaudeau, "A survey of prostate segmentation methodologies in ultrasound, magnetic resonance and computed tomography images," *Computer methods and programs in biomedicine*, vol. 108, no. 1, pp. 262–287, 2012.
- [58] Y. Yu and S. T. Acton, "Speckle reducing anisotropic diffusion," *IEEE Transactions on Image Processing*, vol. 11, no. 11, pp. 1260–1270, 2002.
- [59] J.-S. Lee, "Digital image enhancement and noise filtering by use of local statistics," *IEEE Transactions on Pattern Analysis and Machine Intelligence*, no. 2, pp. 165–168, 1980.
- [60] K. Krissian, C.-F. Westin, R. Kikinis, and K. G. Vosburgh, "Oriented speckle reducing anisotropic diffusion," *IEEE Transactions on Image Processing*, vol. 16, no. 5, pp. 1412–1424, 2007.
- [61] G.-H. Cottet and M. E. Ayyadi, "A Volterra type model for image processing," *IEEE Transactions on Image Processing*, vol. 7, no. 3, pp. 292–303, 1998.
- [62] S. Parrilli, M. Poderico, C. V. Angelino, and L. Verdoliva, "A nonlocal sar image denoising algorithm based on lmmse wavelet shrinkage," *IEEE Transactions on Geoscience and Remote Sensing*, vol. 50, no. 2, pp. 606–616, 2012.

- [63] J. Zhang, C. Wang, and Y. Cheng, "Comparison of despeckle filters for breast ultrasound images," *Circuits, Systems, and Signal Processing*, vol. 34, no. 1, pp. 185–208, 2015.
- [64] W. K. Pratt, *Digital Signal Processing*. Wiley, New York, 1977.
- [65] Z. Wang, A. C. Bovik, H. R. Sheikh, and E. P. Simoncelli, "Image quality assessment: from error visibility to structural similarity," *IEEE Transactions on Image Processing*, vol. 13, no. 4, pp. 600–612, 2004.
- [66] C. T. Vu, T. D. Phan, and D. M. Chandler, "S3: A Spectral and Spatial Measure of Local Perceived Sharpness in Natural Images," *IEEE Transactions on Image Processing*, vol. 21, no. 3, pp. 934–945, 2012.
- [67] P. Jaccard, "Distribution de la flore alpine dans le bassin des dranses et dans quelques régions voisines," *Bull Soc Vaudoise Sci Nat*, vol. 37, pp. 241–272, 1901.
- [68] G. Gerig, M. Jomier, and M. Chakos, "Valmet: A new validation tool for assessing and improving 3D object segmentation," in *Medical Image Computing and Computer-Assisted Intervention—MICCAI 2001*. Springer, 2001, pp. 516–523.
- [69] M. Soret, S. L. Bacharach, and I. Buvat, "Partial-volume effect in PET tumor imaging," *Journal of nuclear medicine : official publication, Society of Nuclear Medicine*, vol. 48, no. 6, p. 932–945, June 2007. [Online]. Available: <https://doi.org/10.2967/jnumed.106.035774>
- [70] K. Erlandsson, I. Buvat, P. H. Pretorius, B. A. Thomas, and B. F. Hutton, "A review of partial volume correction techniques for emission tomography and their applications in neurology, cardiology and oncology," *Phys Med Biol*, vol. 57, no. 21, pp. R119–159, Nov 2012.
- [71] N. Bousson, M. Hatt, F. Lamare, Y. Bizais, A. Turzo, C. Cheze-Le Rest, and D. Visvikis, "A multiresolution image based approach for correction of partial volume effects in emission tomography," *Physics in medicine and biology*, vol. 51, pp. 1857–1876, Apr. 2006.
- [72] B. A. Thomas, K. Erlandsson, M. Modat, L. Thurfjell, R. Vandenberghe, S. Ourselin, and B. F. Hutton, "The importance of appropriate partial volume correction for PET quantification in Alzheimer's disease," *Eur. J. Nucl. Med. Mol. Imaging*, vol. 38, no. 6, pp. 1104–1119, Jun 2011.
- [73] J. Tohka and A. Reilhac, "Deconvolution-based partial volume correction in Raclopride-PET and Monte Carlo comparison to MR-based method," *Neuroimage*, vol. 39, no. 4, pp. 1570–1584, Feb 2008.
- [74] N. Bousson, C. Cheze Le Rest, M. Hatt, and D. Visvikis, "Incorporation of wavelet-based denoising in iterative deconvolution for partial volume correction in whole-body PET imaging," *European journal of nuclear medicine and molecular imaging*, vol. 36, pp. 1064–1075, Jul. 2009.
- [75] A. Le Pogam, H. Hanzouli, M. Hatt, C. Cheze Le Rest, and D. Visvikis, "Denoising of pet images by combining wavelets and curvelets for improved preservation of resolution and quantitation," *Medical image analysis*, vol. 17, pp. 877–891, Dec. 2013.
- [76] A. Reilhac, C. Lartizien, N. Costes, S. Sans, C. Comtat, R. N. Gunn, and A. C. Evans, "PET-SORTEO: a Monte Carlo-based Simulator with high count rate capabilities," *IEEE Transactions on Nuclear Science*, vol. 51, no. 1, pp. 46–52, Feb 2004.
- [77] J. Tohka and A. Reilhac, "A monte carlo study of deconvolution algorithms for partial volume correction in quantitative pet," in *2006 IEEE Nuclear Science Symposium Conference Record*, vol. 6, Oct 2006, pp. 3339–3345.



Vincent Jaouen was born in Suresnes, France, in 1985. He received the M.Sc. degree in Applied Physics from the University of Rennes I, Rennes, France, in 2012 and the Ph.D. degree from the University of Tours, Tours, France, in 2016. During his Ph.D., he was a teaching assistant in Signal Processing at National Institute For Applied Sciences (INSA) School of Engineering, Blois, France. He is now a postdoctoral fellow at LaTIM laboratory, Université de Bretagne Occidentale, Inserm, Brest, France. His research interests are in image segmentation and filtering techniques applied to medical images such as PET, dynamic PET, MRI, Ultrasound or Multimodal images.

tion and filtering techniques applied to medical images such as PET, dynamic PET, MRI, Ultrasound or Multimodal images.



Julien Bert was born in St Rémy, Burgundy, France, in 1980. He received the B.S. degree in control, electronic and electrical engineering in 2001, M.S. degree in control and computation engineering in 2004 and Ph.D. degree in control engineering from Franche-Comté University, France, in 2007. From 2007 to 2010, he was postdoctoral fellow with the Houston Medical School, Texas Medical Center, TX, USA. He has been a Hospital Research Engineer with Brest Regional University Hospital in 2010, and since 2012, Principal Hospital Research Engineer.

His permanent position is assigned with the Laboratory of Medical Information Processing INSERM (French National Institute of Health and Medical Research). Since 2013, he has been also on secondment with the Research Institute of Technology B<>COM within the Augmented Healthcare Lab. His main research interest is in image-guided radiotherapy especially in intra-operative radiotherapy treatment. Within this context he is leading a research group working on physics Monte-Carlo simulation, treatment planning optimization and control of treatment delivery systems. He is implicated in several national and European research projects especially in prostate brachytherapy.



Nicolas Bousson was born in 1972 and obtained his PhD in 2001 from the University of Lyon, France, working on functional imaging of epilepsy. He was postdoctoral fellow at the Laboratory of Biorheology and Medical Ultrasonics in Montreal, Canada, and then at INSERM UMR 1101 LaTIM, Brest, France. He obtained his habilitation à diriger des recherches in 2016 and is currently medical physicist in the radiotherapy department of the Brest University Hospital, France. His main research interests focus on image analysis, image fusion, quantitation in

PET imaging, as well as simulation of devices and tumoral processes for radiotherapy applications.



Hadi Fayad With an initial engineering formation in computer sciences (2006), a master (2007) and a PhD in medical image processing (2011), Hadi Fayad was recruited as an assistant professor (2012) at the faculty of medicine at the University of Western Brittany (UBO) and incorporated the LaTIM laboratory (INSERM U1101). His actual research activities deals with motion management in radiotherapy and in multi-modality imaging such as PET/CT and PET/MR. Hadi Fayad is in charge of the SIBM (Signal and Image in Biology and

Medicine) master and is responsible for the computer and internet certificate at the faculty of Medicine of the UBO.



Mathieu Hatt is a junior research associate with the INSERM LaTIM UMR 1101 and is in charge of research activities dedicated to multimodal image analysis and processing for oncology applications, radiomics and predictive modeling. He received his Master degree in computer sciences from the University of Strasbourg in 2004, his PhD degree from the University of Brest in 2008, and his habilitation to supervise research in 2012



Dimitris Visvikis is a Director of research with the National Institute of Health and Medical Research (INSERM) in France. He is co-director of the Medical Image Processing Lab in Brest (LaTIM), where he has been leading a group on quantitative multi-modality imaging for therapy applications. He currently has an appointment as a consultant physicist within the Brest University Hospital, while he has held different principal and consultant MPE positions in the field of Nuclear Imaging in the UK over the last twenty years. Within this context he

has previously led the development of PET and PET/CT clinical units and associated research at the University of Cambridge and University College London, following his PhD in PET hardware development, working within the Institute of Cancer Research and the Royal Marsden Hospital in London. He has spent the majority of his scientific activity in the field of PET and SPECT imaging, including developments in both hardware and software domains. He is a member of numerous professional societies such as IPEM (Fellow, past Vice-President International), IEEE (Senior Member), AAPM, SNM (CaIC board of directors 2007-2012), EANM (physics committee, 2017-), EFOMP (Examinations board, Projects committee). He was chair of the IEEE NPSS Nuclear Medical Imaging Sciences Committee (2013- 2015), MIC program chair for the 2016 NSS/MIC conference in Strasbourg and he is the current Editor-in-Chief of the new NPSS journal "IEEE Transactions in Radiation and Plasma Medical Sciences".